AGU PUBLICATIONS

JGR

Journal of Geophysical Research: Atmospheres

RESEARCH ARTICLE

10.1002/2015JD023872

Key Points:

- Diurnal cycle of convection over PRD during Mei-Yu season
- Propagation of convection
- Mechanisms of nocturnal convection

Correspondence to:
K. Zhao,
zhaokun@nju.edu.cn

Citation:
Chen, X., K. Zhao, M. Xue, B. Zhou, X. Huang, and W. Xu (2015), Radar-observed diurnal cycle and propagation of convection over the Pearl River Delta during Mei-Yu season, *J. Geophys. Res. Atmos.*, *120*, 12,557–12,575, doi:10.1002/2015JD023872.

Received 29 JUN 2015
Accepted 25 NOV 2015
Accepted article online 27 NOV 2015
Published online 28 DEC 2015

Radar-observed diurnal cycle and propagation of convection over the Pearl River Delta during Mei-Yu season

Xingchao Chen[1], Kun Zhao[1], Ming Xue[1,2], Bowen Zhou[1], Xuanxuan Huang[1], and Weixin Xu[3]

[1]Key Laboratory for Mesoscale Severe Weather/MOE and School of Atmospheric Science, Nanjing University, Nanjing, China, [2]Center for Analysis and Prediction of Storms and School of Meteorology, University of Oklahoma, Norman, Oklahoma, USA, [3]Department of Atmospheric Sciences, Colorado State University, Fort Collins, Colorado, USA

Abstract Using operational Doppler radar and regional reanalysis data from 2007–2009, the climatology and physical mechanisms of the diurnal cycle and propagation of convection over the Pearl River Delta (PRD) region of China during the Mei-Yu seasons are investigated. Analyses reveal two hot spots for convection: one along the south coastline of PRD and the other on the windward slope of mountains in the northeastern part of PRD. Overall, convection occurs most frequently during the afternoon over PRD due to solar heating. On the windward slope of the mountains, convection occurrence frequency exhibits two daily peaks, with the primary peak in the afternoon and the secondary peak from midnight to early morning. The nighttime peak is shown to be closely related to the nocturnal acceleration and enhanced lifting on the windward slope of southwesterly boundary layer flow, in the form of boundary layer low-level jet. Along the coastline, nighttime convection is induced by the convergence between the prevailing onshore wind and the thermally induced land breeze in the early morning. Convection on the windward slope of the mountainous area is more or less stationary. Convection initiated near the coastline along the land breeze front tends to propagate inland from early morning to early afternoon when land breeze cedes to sea breeze and the prevailing onshore flow.

1. Introduction

The diurnal cycle is one of the most fundamental modes in the Earth climate system. Characterizing the diurnal cycle and propagation of convective storms can help us understand not only the initiation and evolution mechanism of convection but also the mechanism that drives the local climate. It also can be used as an evaluation bench mark for convective-scale numerical weather prediction models and for quantitative precipitation forecasts. Therefore, the diurnal variation and propagation of convection over different geographic regions have been receiving much attention in recent years [*Carbone et al.*, 2000; *Lang et al.*, 2007; *Carbone and Tuttle*, 2008; *He and Zhang*, 2010; *Romatschke et al.*, 2010; *Bao et al.*, 2011; *Sun and Zhang*, 2011; *Chen et al.*, 2012, 2014a]. Besides the diurnal variation of solar heating, the regular occurrence of convection and precipitation at particular times of day is also connected to regional and large-scale orography, including land-sea contrasts, local land use/land cover, and atmospheric circulation pattern and thermodynamic conditions [*Yang and Slingo*, 2001; *Chen et al.*, 2012; *Yuan et al.*, 2012]. Therefore, diurnal cycles of convective precipitation often vary markedly from region to region and require specific studies.

Diurnal cycles of convective precipitation have been investigated in various regions of the world, by using surface station, weather radar, satellite imagery, and lightning observations. *Wallace* [1975] used data from more than 100 surface stations to investigate the diurnal cycles of all types of precipitation events in the U. S. He found, over the central United States, that severe convective storms initiate mostly during the early evening and exhibit their maximum frequency around midnight. *Iwasaki et al*. [2008] studied the diurnal variations of convective rainfall around Ulaanbaatar, Mongolia, based on data from C band airport radar and GPS receivers. In this arid region, convective activity exhibits a pronounced diurnal cycle with a peak at early afternoon. *Nesbitt and Zipser* [2003] used 3 year Tropical Rainfall Measuring Mission (TRMM) Precipitation Radar and TRMM Microwave Imager measurements to investigate the diurnal cycle of rainfall and convective intensity over tropical land and ocean. They found that the diurnal cycle of precipitation over ocean area has smaller amplitudes than that over land. *Yang and Smith* [2008] used 8 years of TRMM data to document the seasonal diurnal variability of convective and stratiform rainfall in the tropics. They found that oceanic (continental) convective rainfall was up to 25% (50%) greater during nighttime (daytime) than daytime (nighttime) in the tropics. *Watson et al*. [1994] used 6 years of cloud-to-ground lightning data to investigate diurnal cycles of thunderstorms in Arizona during the Southwest Monsoon. Results show that moisture conditions, location of the subtropical ridge, transitory troughs in both the westerlies and easterlies, and low-level moisture surges from the Gulf of California play various roles in the diurnal cycles of convective rainfall and lightning production in Arizona.

In recent years, diurnal cycle of precipitation in China, especially during the warm season, also received much attention based on surface, radar, and satellite observations [*Chen et al*., 2009; *He and Zhang*, 2010; *Yu et al*., 2010; *Bao et al*., 2011; *Sun and Zhang*, 2011; *Xu and Zipser*, 2011; *Chen et al*., 2012; *Luo et al*., 2013; *Zhao*, 2013; *Chen et al*., 2014a]. During the warm season, there are three rainfall centers or maximum rainfall regions in China: South China, Yangtze-Huai River Basin, and North China [*Ding and Chan*, 2005]. Convective rainfall is believed to be the major contributor to the total warm season precipitation in these three regions [*Liu and Fu*, 2010; *Yu et al*., 2010; *Chen et al*., 2012; *Luo et al*., 2013; *Chen et al*., 2014b]. These regions exhibit different diurnal cycles in the warm season precipitation as revealed by long-term hourly rain gauge observations, probably due to difference in atmospheric environments and topographies [*Yu et al*., 2007].

With increasing number of observations, several mechanisms explaining the diurnal cycle of precipitation have been proposed for the Yangtze-Huai River Basin and North China [*Johnson et al*., 2010; *Yuan et al*., 2012]. *Bao et al*. [2011] found that diurnal cycle of precipitation in the Yangtze-Huai River Basin can be simultaneously influenced by the solar heating, eastward propagation of precipitation systems, and regional mountain-plains solenoids. *Chen et al*. [2010] suggested that the eastward delayed initiation of the nocturnal long-duration rainfall events in the Yangtze-Huai River Basin is due to the diurnal clockwise rotation of the low-tropospheric circulation, especially the accelerated nocturnal southwesterly. *He and Zhang* [2010] examined the diurnal variations of the warm season precipitation over northern China and found that the diurnal precipitation peak (trough) is closely collocated with the upward (downward) branch of a mountain-plains solenoidal circulation. *Chen et al*. [2014a] also found that the diurnal evolution and distribution of warm season convective storms over North China can be influenced by different prevailing wind regimes on the 925 hPa and 500 hPa levels.

Compared to Yangtze-Huai River Basin and North China, mechanisms of diurnal cycles in South China are less known, especially for the Pearl River Delta (PRD) region. The PRD, as one of the maximum rainfall centers [*Xu et al*., 2009], is a population and economic center in South China. *Chen et al*. [2014b, hereinafter C14] used 3 years of Doppler radar data to investigate the diurnal variation, intensity, and spatial distribution of convection over the PRD during the warm season. Their study shows that convective precipitation can contribute to more than 50% of the total rainfall. They also found profound monthly variations of the diurnal cycle of convection. During late summer (July and August), convection occurs mostly in the early afternoon due to solar heating effect. During the Mei-Yu Season (May to June, also called "presummer rainy season of South China"), a second convective precipitation peak is found in the early morning. C14 documented this secondary peak but did not explain its physical mechanism. In addition, PRD exhibits strong subregional (e.g., mountainous versus coastal area) variability in convective characteristics. How and why the diurnal cycles vary with the geographic location remain to be understood. It is the goal of this paper to address these questions. Specifically, the diurnal cycle and propagation of convection over PRD during the Mei-Yu seasons are studied using three Mei-Yu seasons data from an operational weather radar. Sounding data and the Japan Meteorological Agency (JMA) regional gridded reanalysis data are used to examine the diurnal changes of associated meteorological conditions, including flow patterns and thermodynamic properties. Different from earlier studies based on polar-orbiting satellite data, this paper takes advantage of the high temporal and spatial resolutions of ground-based radars to reveal detailed variations in diurnal cycle and propagation over PRD during the Mei-Yu seasons. We also offer explanations on the underlying physical mechanisms of the diurnal cycles and propagation of convection in this region.

The rest of the paper is organized as follows: data and methodology are introduced in section 2. Section 3 presents an overview of Mei-Yu conditions during 2007–2009. Diurnal cycle and propagation of convection for the region, together with their mechanisms, are discussed in section 4. Summary and conclusions are given in section 5.

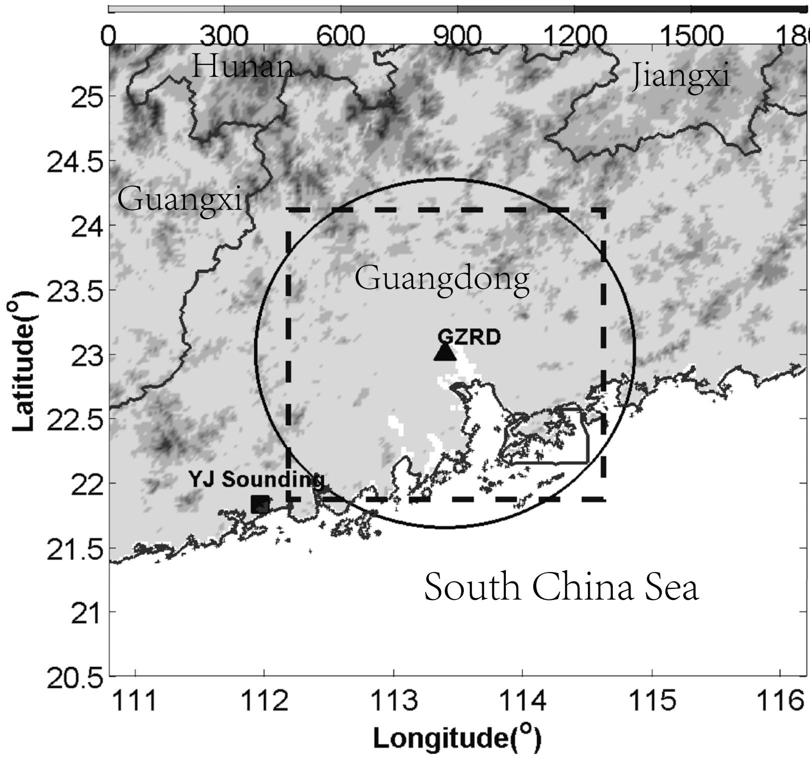

Figure 1. Locations of the Guangzhou radar (GZRD) and Yangjiang (YJ) sounding station (black square). Pearl River Delta (PRD) is marked by dashed square. Orography is shown in gray scale. Coastlines and provincial borders are shown, together with the 150 km range circles of the GZRD.

2. Data and Methods

2.1. Radar Data

The radar data used in this study are collected from China's Weather Surveillance Doppler-1998 radar at Guangzhou (GZRD in Figure 1), operated by the China Meteorological Administration (CMA). The GZRD is located in the center of the PRD region. Its coverage area is characterized as a plain surrounded by moderate-height (400–800 m) mountains on the north and the coastline to the south. Data from GZRD are used to investigate the diurnal cycle and propagation of convection over PRD. The data set covers the 2007 to 2009 Mei-Yu seasons. There were no tropical cyclones (TCs) near PRD during our analysis period, so the effect of TCs can be excluded in this study.

The GZRD system has a calibration precision of 1 dB through calibrating reflectivity for every volume scan using internally generated test signals. Contaminated radar reflectivity due to ground, mountain, or sea clutters was removed, and aliased velocity data were unfolded using an automatic quality control procedure following *Zhang et al.* [2004] and *Zhang and Wang* [2006]. After the quality control, the reflectivity data were bilinearly interpolated onto constant altitude plan position indicators in Cartesian coordinates with a 1 km grid spacing in both horizontal and vertical [*Mohr and Vaughan*, 1979]. The Cartesian-based radar volumes cover 150 km × 150 km horizontally and 15 km vertically every 6 min. More details on the radar data and the quality control and interpolation procedures can be found in C14.

2.2. Classification of Convective Precipitation and Radar Quantitative Precipitation Estimation

An algorithm based on *Steiner et al.* [1995] is applied to the Cartesian-gridded reflectivity data of GZRD at 3 km altitude to identify convective and stratiform precipitation. As described in C14, the first step of classification is to label all grid points with a reflectivity of at least 40 dB*Z* as convective. Then, grid points with reflectivity exceeding the average value within an 11 km radius of a convective grid point labeled as such in the first step by a specified amount (this criterion is given in Figure 7 of *Steiner et al.* [1995]) are also identified as convective. Finally, for each convective grid point, all surrounding grid points within an

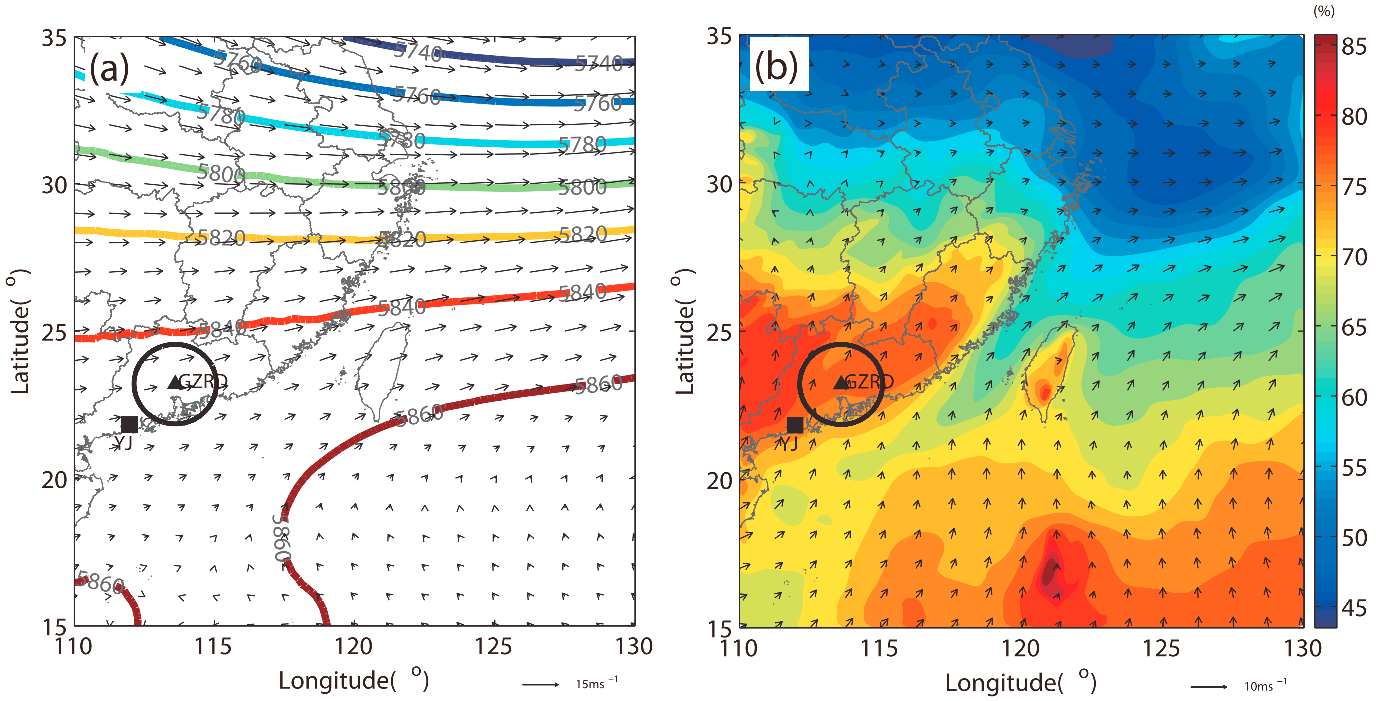

Figure 2. (a) The mean pressure (contours) and wind (arrow) fields at 500 hPa and (b) the relative humidity (color-filled contours) and wind (arrows) fields at 850 hPa based on JMA reanalysis data for three Mei-Yu seasons (from 11 May to 24 June). The Yangjiang sounding station is represented by the black square. The Guangzhou radar is represented by the black triangle. The radar coverage area (150 km) is indicated by the black circle.

intensity-dependent radius are also identified as convective. More details on the classification procedure can be found in C14.

Radar-based quantitative precipitation estimation (QPE) can be affected by inappropriate radar reflectivity-rainfall rate (*Z-R*) relationships, range dependence, beam blockage, and other uncertainties [*Parker and Knievel*, 2005]. To improve radar QPE, different *Z-R* relations, similar to *Xu et al*. [2008], are used to estimate convective and stratiform precipitation intensity. For convective precipitation, the relationship of $Z = 32.5R^{1.65}$ adopted by the Taiwan Central Weather Bureau (http://www.cwb.gov.tw/) during monsoon season is used. *Wang et al*. [2014] compared the QPE obtained using the above relationship with rain gauge data over PRD and found it to be reasonably accurate. For stratiform precipitation, $Z = 200R^{1.6}$ [*Marshall and Palmer*, 1948] is applied. QPEs of convective and stratiform precipitation are calculated based on radar reflectivity on the lowest 0.5° elevation. The melting layer over PRD during Mei-Yu seasons is around 5 km [*Chen et al*., 2014b]; the contamination from bright band should be very small if any. Based on 10 years of TRMM observations, *Xu et al*. [2009] found that the radar reflectivity profiles of convective rainfall below 5 km height does not change much during the Mei-Yu season, so the impact of reflectivity variation with height on radar QPE should be small. Furthermore, radar beam blockage appears to affect only a few radials in northeast mountainous areas of GZRD, so its impact on radar QPE is also small. The QPEs for convective and stratiform rain are then accumulated separately at each grid point for the three years. The total rainfall refers to the sum of these two types of rainfall.

2.3. Additional Data

Sounding data (twice a day, at 00 and 12 UTC) collected from Yangjiang (marked as YJ in Figure 2) is used to define the low-level jet (LLJ) periods during the Mei-Yu season. Japan Meteorological Agency (JMA) East Asia reanalysis data sets are used to characterize the large-scale conditions over the area of interest and examine possible mechanisms of certain diurnal cycle patterns in PRD. These reanalysis data have a horizontal resolution of 0.25° by 0.2° and are available at 0000, 0600, 1200, and 1800 UTC (0800, 1400, 2000, and 0200 local standard time (LST)) each day [*Saito et al*., 2006].

3. Overview of Mei-Yu During 2007–2009

3.1. Environmental Conditions

Associated with the onset of the Asian summer monsoon, moisture coming from South China Sea and Indian Ocean reach South China during the Mei-Yu season, leading to a dramatic change in climate regime in East Asia. The Mei-Yu season in South China marks the beginning of summer monsoon over China [*Ding and Chan*, 2005]. The onset occurs in mid-May and is associated with a rapid increase in deep convection and rainfall over South China. Heavy rainfall occurs frequently and causes severe flooding and land sliding during this season [*Chen*, 1993; *Johnson and Ciesielski*, 2002]. The persistent precipitation is usually associated with the weather system called Mei-Yu front (also called "South China quasi-stationary front" [*Ding*, 1994]). Mei-Yu front is characterized as a synoptic frontal system with strong moisture gradients and horizontal wind shears. It usually regulates a widespread precipitation rainband over East Asia. *Xu et al.* [2009] used 10 year TRMM version-6 3B42 data to define Mei-Yu rainband. Statistics of the Mei-Yu rainbands indicate that most of the rainbands develop to the south of the Yangtze River during 11 May to 24 June. This period is then defined as the Mei-Yu season in South China and Taiwan. This definition is adopted for this study, and all subsequent analyses are focused on this period.

The mean synoptic maps of the Mei-Yu seasons of 2007–2009 at the 500 and 850 hPa levels are shown in Figure 2. The 500 hPa height field is typically used to identify the west Pacific subtropical high (WPSH), while the 850 hPa level fields indicate important low-level flow features associated with Mei-Yu systems. Figure 2a shows that the WPSH ridge is located at 19°N and west-southwest winds dominate over the PRD during the Mei-Yu season. At the 850 hPa level, warm moist air is brought in from the ocean by the prevalent southwest flows, resulting in a relative humidity of over 75% over the PRD (Figure 2b). This southwest monsoon flow is closely related to the high pressure-gradient between the WPSH and the monsoon trough located to its west [*Chen and Chang*, 1980; *Rodwell and Hoskins*, 2001].

Figure 3 presents the time series of the 850 hPa level wind speed component during each of the 2007–2009 Mei-Yu seasons as observed by Yangjiang sounding. The positive and negative winds represent flows from the south and north, respectively. Strong low-level southerly exceeding 12.5 m s^{-1}, or the LLJ, mostly occur within the period when the Mei-Yu front is over South China, as indicated by the red sections of the curves. The location of the Mei-Yu front is determined by daily surface and upper level (850, 700, 500, and 200 hPa) weather maps from CMA. This cooccurrence of LLJ and Mei-Yu front has been documented in many previous studies. The LLJ south of the Mei-Yu front can bring strong southwesterly monsoon flows to south China and create favorable conditions for active mesoscale convective systems [*Chen and Yu*, 1987; *Cho and Chen*, 1995; *Chen et al*., 1998; *Jou and Deng*, 1998; *Chen et al*., 2004; *Chang et al*., 2009; *Xu et al*., 2009].

3.2. Spatial Distributions of Precipitation

The spatial distribution of the accumulated occurrence frequency (OF) of convection during the 2007–2009 Mei-Yu seasons is presented in Figure 4a. The OF at each point is counted as the total number of times that a particular grid point is recognized as a convective grid point. During Mei-Yu season, the OF maxima are generally found on the windward (the prevailing winds being southwesterly) slope of the northeastern mountainous region (region B) and along the southern coastal area (region C). The OF minimum is located at the west side of the PRD, which is on the leeside of the prevailing low-level southwesterly winds (region A). This spatial distribution pattern is largely similar to that of the entire warm season as documented in C14. The difference is that convection occurs more frequently on the southern windward slope of mountainous region over the entire warm season while more frequently on the southwest windward slope in Mei-Yu season. This is because the low-level prevailing wind direction is southwesterly during the Mei-Yu season but southerly during the summer.

The spatial distribution of the accumulated convective rainfall in PRD over the three Mei-Yu seasons is shown in Figure 4b (The underestimation of rainfall along a few rays behind the northeast mountainous areas is due to beam blockage). In general, the spatial patterns of total convective rainfall correspond well with the OF of convection. Two convective rainfall maxima are identified: one located along the coastal area (region C) and the other on the windward slope of the northeastern mountains (region B). Compared with the convective rainfall, stratiform rainfall amount is much smaller (Figure 4c), and the spatial distribution is rather uniform. Contribution of convective rainfall to total rainfall is relatively high in the maximum rainfall regions B and C (Figure 4d).

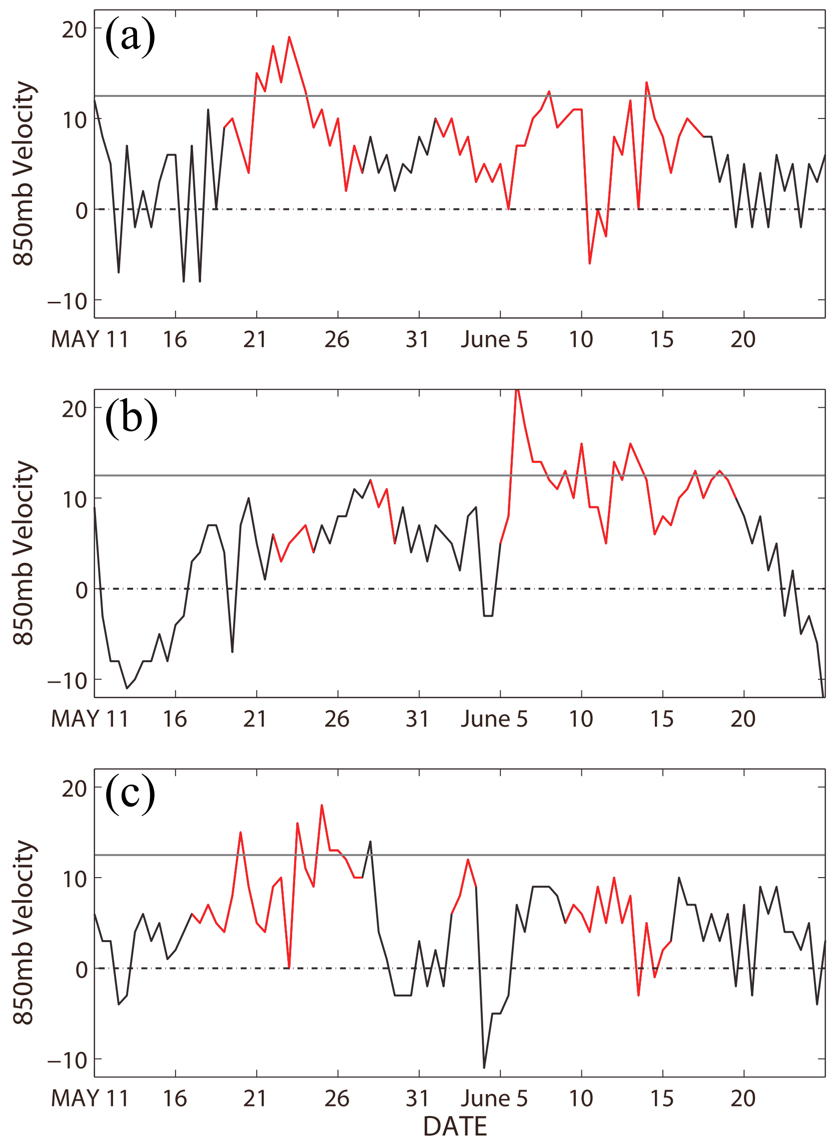

Figure 3. North-south velocity component at 850 hPa from Yangjiang sounding during (a) 2007, (b) 2008, and (c) 2009 Mei-Yu seasons. Sections of the curves are marked red when the Mei-Yu front is found in South China during the time. The solid black lines indicate 12.5 m s^{-1} southerly wind.

4. Diurnal Cycle and Propagation of Precipitation

In this section, the diurnal cycle of precipitation during Mei-Yu season in PRD is studied. We further examine the diurnal cycles of precipitation in three subregions (regions A–C in Figure 4), propagation of convection, and possible mechanisms of nighttime and early morning convection.

4.1. Diurnal Cycle of Precipitation

The diurnal cycles of average total rainfall and convective and stratiform precipitation per grid point of the PRD and its three subregions during the three Mei-Yu seasons are shown in Figure 5. The rain rate at each grid point is calculated by the *Z-R* relations introduced in section 2.2. Rainfall in PRD reaches its maximum in the afternoon around 1600 LST. A relatively weak peak in the early morning around 0600 LST is also discernable.

Because Mei-Yu precipitation is mostly (more than 70%) contributed by convective rainfall (Figure 4d), the diurnal variation of convective precipitation (not shown) is almost identical to that of total rainfall.

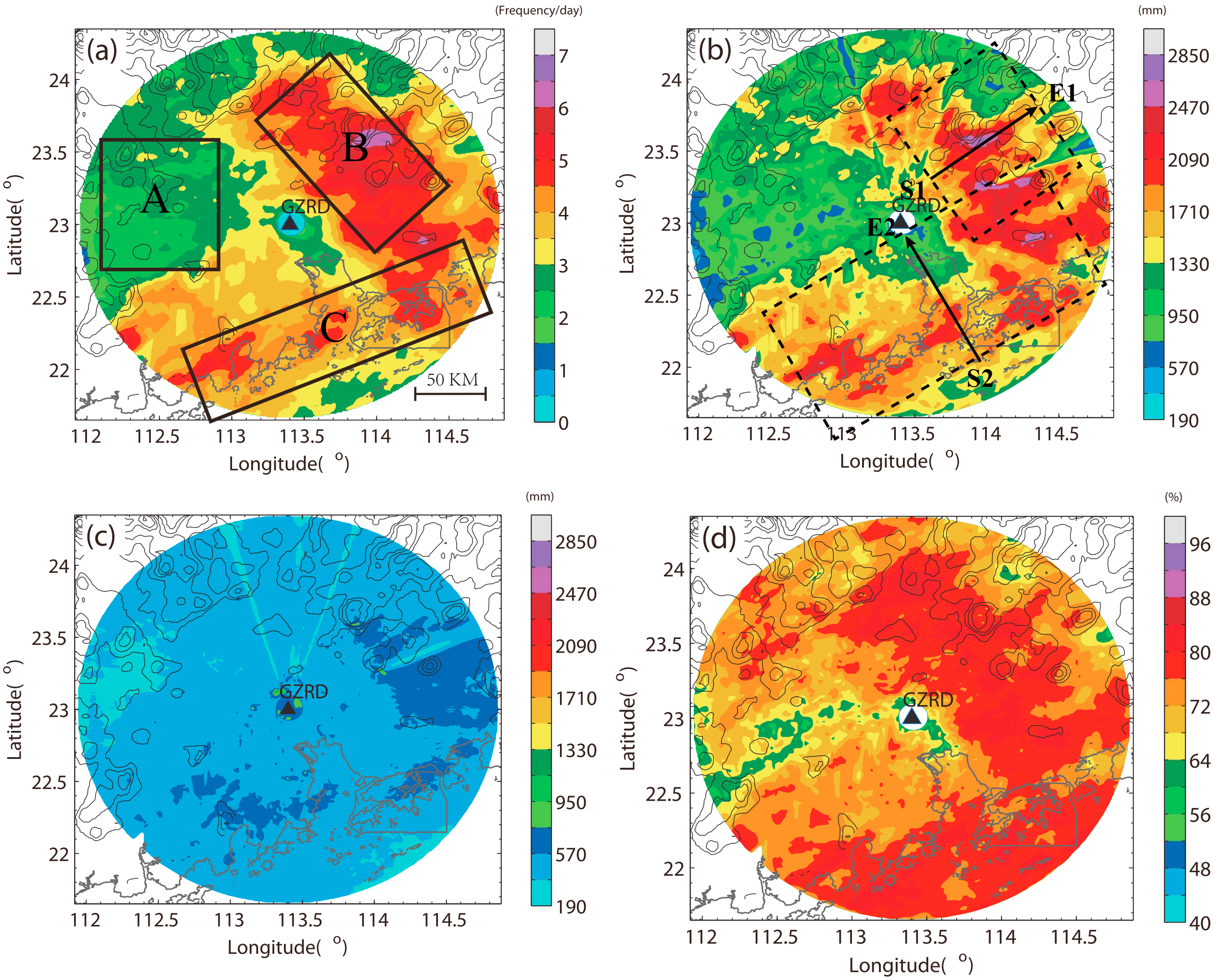

Figure 4. The spatial distributions of (a) the occurrence frequency per day of convective grid point, (b) accumulated convective rainfall, (c) accumulated stratiform rainfall, and (d) percentage of convective rainfall events during 2007–2009 Mei-Yu seasons. Orography is superimposed as black contours at 150 m intervals. Fifty kilometer spatial scale bar is shown in Figure 4a.

Specifically, region A is dominated by the afternoon (mostly convective) rainfall that peaks at 1600 LST. This peak is closely related to the solar-heating-induced convective precipitation [*Romatschke and Houze*, 2011; *Chen et al*., 2014b]. Convective precipitation in region B shows a clear early morning (around 0600 LST) peak, in additional to the early afternoon (1300 LST) peak. The earlier onset of afternoon convection in region B is possibly due to the help of upslope flow induced by heating to the elevated mountain surfaces.

The physical mechanism behind the early morning peak in region B is worth investigating. Inland nocturnal convection can be induced by various processes including convergence between nighttime downslope drainage flow and moist monsoon flow that had been observed at the foot of the Himalayas during South Asian monsoon [*Romatschke and Houze*, 2011], nocturnal LLJ-induced convection over the U.S. Great Plains [*Astling et al*., 1985], and eastward propagation of convective systems from the Tibetan Plateau over east China during the warm season [*Bao et al*., 2011]. Possible mechanisms responsible for the early morning rainfall peak in region B will be discussed in section 4.3.

The diurnal cycle of convective precipitation in region C is distinct from that of regions A and B. The convective rainfall in region C peaks at late morning (1000–1100 LST) and reaches a minimum in the evening (around 2000 LST). This diurnal characteristics is similar to the observations of the Hawaiian Rainband Project;

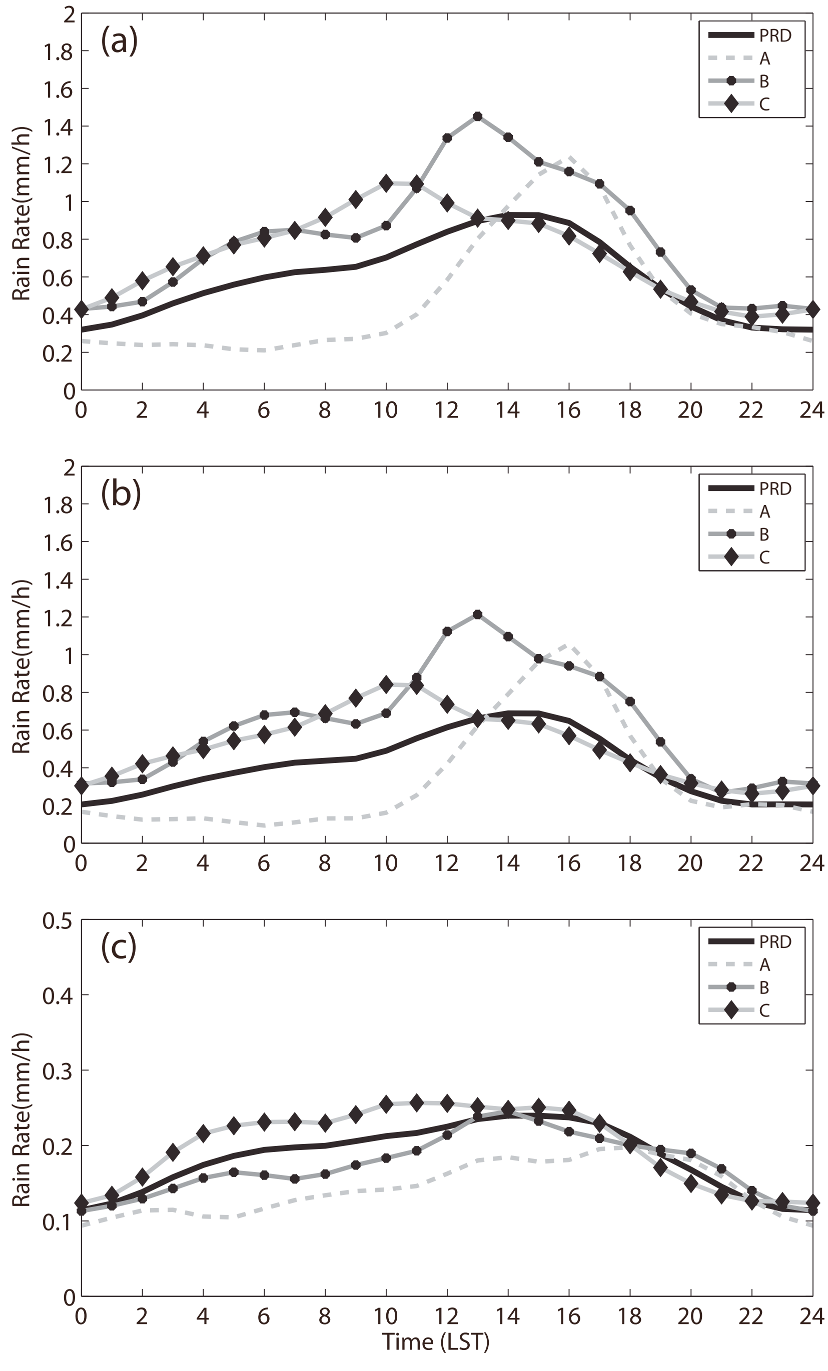

Figure 5. Time series of average (a) total rain rate, (b) convective rain rate, and (c) stratiform rain rate over the PRD and three subregions during the 2007–2009 Mei-Yu seasons. Note that the *y* axis of Figure 5c is different from those of Figures 5a and 5b.

coastal precipitation on the windward side of Hawaii occurs mostly in the predawn and early morning hours (0300–1100 LST), and this rainfall maximum is related to the local rain showers and onshore drifting of rainbands [*Chen and Feng*, 1995]. Further analysis on the coastal convection in the PRD will be given in the section 4.3.

Diurnal cycles of stratiform rainfall over the PRD and the three subregions are shown in Figure 5c. Compared with convective rainfall, the diurnal variations of stratiform precipitation are much milder, and the percentage of morning rainfall to the total rainfall is higher than the convective rainfall case. In addition, there is a clear phase shift of the afternoon peak between convective (Figure 5b) and stratiform (Figure 5c) rainfall in the two inland regions (A and B). In these regions, stratiform rainfall peaks 1–2 h after the maximum convective rainfall. This may be because stratiform precipitation is what remains when strong convection dies out and most of the convective instability is released, but the exact reason will require further study. In comparison, the high stratiform rainfall in the coastal region C shows a more flat pattern, with no clear peak. The intensity of stratiform rainfall is much weaker than convective rainfall (also see Figure 4). During the Mei-Yu season, stratiform precipitation only accounts for around 20%–25% of the total rainfall over the PRD (Figure 4d), which is consistent with the finding of *Liu and Fu* [2010] based on 10 year TRMM radar data for southern China. The diurnal variation of total rainfall is mainly contributed by convective precipitation. Therefore, the rest of this paper will focus on the diurnal variation and propagation of convection in the PRD.

Figure 6 shows the spatial distribution of convective OF averaged over 1 h periods at every 3 h, during the Mei-Yu season. Convection starts to develop along the coastline (region C) and on the windward slope of the eastern mountainous region (region B) at 0000 LST. Convective population keeps increasing in the next few hours in these two subregions and reaches a temporary peak around 0600 LST. After sunrise (0900 LST), convection in region B dissipates to some extent. Convection in region C keeps developing until 1100 LST (not shown in Figure 6) and tends to propagate from the coast inland with time. After 1200 LST, region B experiences dramatic growth of convective population probably due to increased solar heating. In the meantime, convective population along the coastline decreases significantly and becomes much less than inland areas. After sunset (1800 LST), convective population in all regions (A–C) decreases. By 2100 LST, few convective cells remain. In general, the diurnal variations seen in these plots match those seen in Figure 5, but these plots offer additional insight on the spatial propagation of convection, which will be discussed next.

4.2. Propagation of Convection

Daily Hovmöller diagrams of the hourly averaged convection OF are plotted in Figure 7. Figure 7a is aligned along the width of the dashed rectangle marked with S1 and E1 in Figure 4b and averaged along the cross direction. It approximates a southwest to northeast orientation (SW-NE). Two OF maxima are present on the windward slope of this region. The first one is around 0600 LST, and the second is from 1000 to 1700 LST, consistent with the time series plots in Figure 5. Both maxima are more or less quasi-stationary, although the latter one has some northeast propagation. The early morning high-OF region is located only on the windward slope, while the late morning to afternoon high-OF region can be found above the mountainous region as well as over the lower plains. Such distributions suggest that the early morning convection is triggered by the mountain slope in the presence of southwesterly flows, while the late morning to afternoon convection is due to afternoon maximum solar heating, which is more effective in triggering convection over the mountain slope when elevated heating over the mountains help set up upslope solenoidal circulations.

The Hovmöller diagram in Figure 7b corresponds to the coastal region in Figure 7b. Its spatial dimension is aligned along S2-E2 line in Figure 7b and spatially averaged along the long dimension of the dashed rectangle. It can be seen from Figure 7b that convection starts to initiate along the coastline at around 0200 LST then moves inland form early morning to early afternoon. The inland propagation speed is close to 8 km/h. The propagation slows down at around 80 km in the diagram or about 60 km inland from the coast. At that point, the peak merges with the inland early afternoon convection frequency maximum at around 1500 LST, and the convection dies out quickly after 1700 LST. This propagation feature is very similar to that seen in long-term TRMM observations [*Zhao*, 2013]. How coastal early morning convection is triggered in the PRD in a statistical sense is investigated in the next section.

4.3. Mechanisms of Convection Initiation and Propagation

To understand the possible mechanisms of early morning convection in regions B and C, the diurnal changes of environmental flow and other atmospheric conditions are investigated. Based on the JMA regional reanalysis data set, mean wind and temperature fields during the Mei-Yu seasons at 0200, 0800, 1400, and 2000 LST are shown in Figure 8 for the 900 hPa level and the surface.

Figures 8a–8d show diurnal variations of the wind fields at 900 hPa. In the region, the average prevailing winds at this level are southerly, and the wind speed over land is highest at 0200 and lowest at 1400 LST among the four times shown (Figures 8a and 8c). The wind speed minimum at 1400 LST should be due to

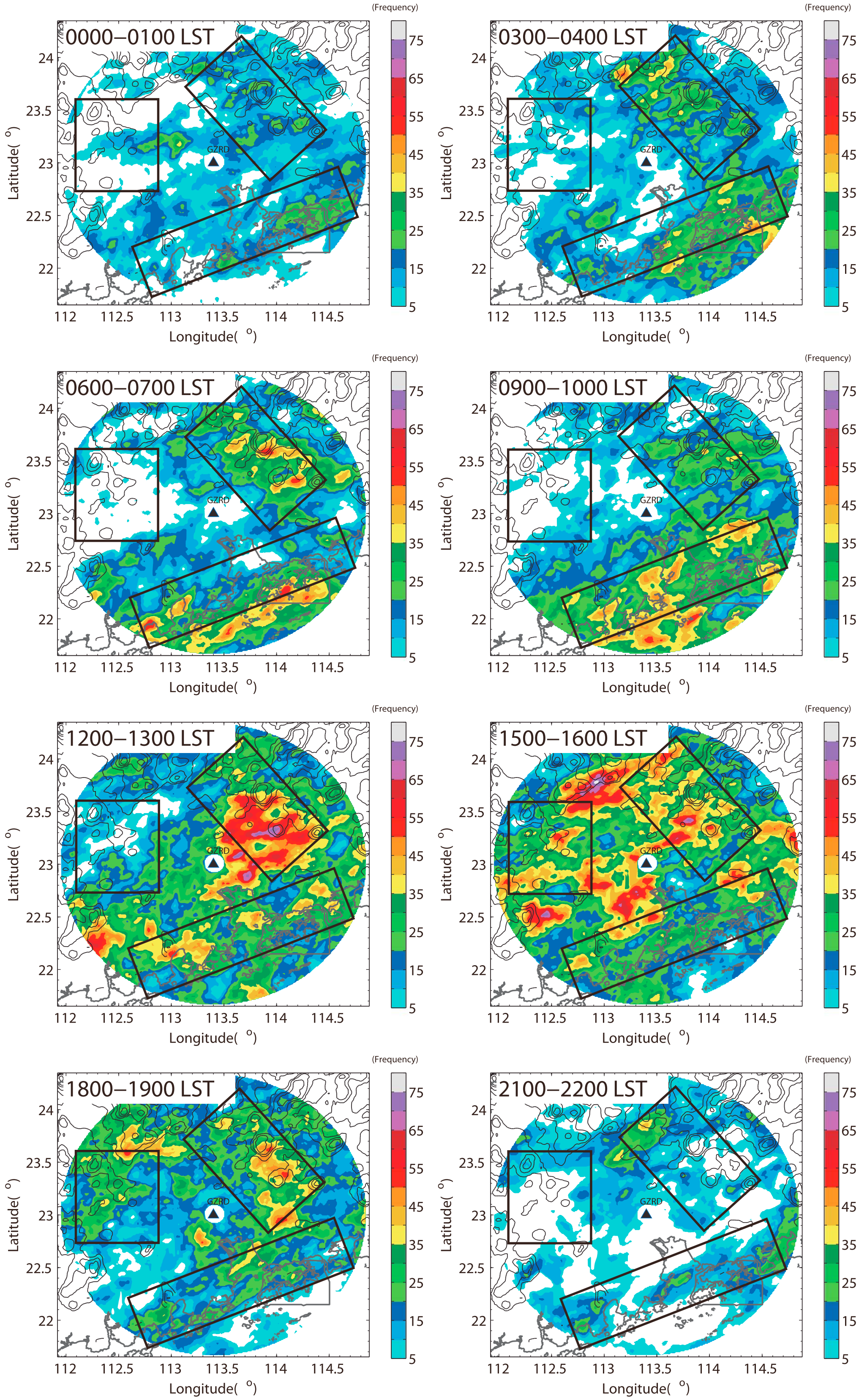

Figure 6. Spatial distributions of convection occurrence frequency between 0000 and 0100, 0300 and 0400, 0600 and 0700, 0900 and 1000, 1200 and 1300, 1500 and 1600, 1800 and 1900, and 2100 and 2200 LST during the 2007–2009 Mei-Yu seasons. Orography is superimposed in the figure in black contours with 150 m intervals.

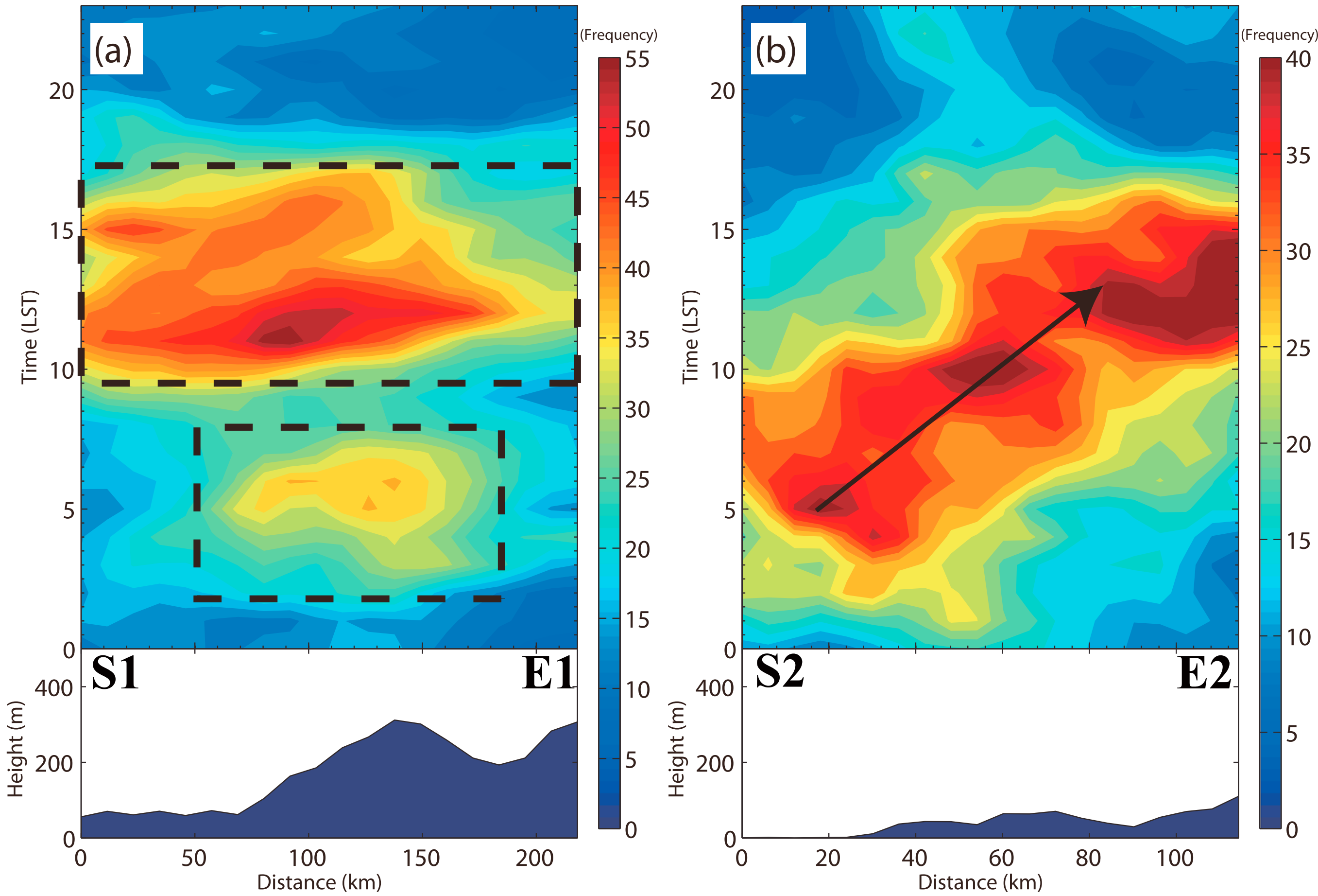

Figure 7. Hovmöller diagrams of mean hourly occurrence frequency of convection along direction (a) S1-E1 and (b) S2-E2, averaged along the other direction of the dashed line boxes shown in Figure 3b. The interpolated topographic profiles along S1-E1 and S2-E2 are shown in the bottom panels.

enhanced vertical mixing in the boundary layer in the afternoon that brings lower momentum air from below to this level, while at night this effect is greatly diminished. At the same time, we can also see a clockwise turning of wind vectors over land from early afternoon to night into early morning (Figures 8c to 8d, 8a, and 8b), maximizing the southwesterly wind component (along dashed line a-b) in the early morning.

The diurnal changes in the wind fields can be seen more clearly by plotting the wind vector differences between 0200 and 2000 LST (Figures 9a and 9c) and between 1400 and 0800 LST (Figures 9b and 9d). At 900 hPa, the most evident change is the great enhancement of the southwesterly winds. This is due to the development of the nocturnal boundary layer low-level jet (LLJ). The LLJ typically forms at the top of the nighttime stable boundary layer as a result of the decoupling of the free atmospheric flow with the boundary layer [*Blackadar*, 1957]. The nocturnal jet is in the general direction of geostropheric winds, which are generally southwesterly above the boundary layer (not shown). The upslope lifting effect of this southwesterly boundary layer jet is believed to be the cause for the early morning precipitation maximum on the windward slope of mountains (Figure 7a). The difference vectors between 1400 and 0800 LST (Figure 9b) are reversed in direction from those between 0200 and 2000 LST (Figure 9a), due to the weakening of southwesterly flow in the afternoon.

Figures 8e–8h show the surface wind and temperature fields at four times of the day. It is clear that there is a large diurnal variation in temperature over land, with the lowest temperature found at 0200 LST and the highest at 1400 LST. The temperature at 1400 LST over ocean is also the highest, but the diurnal variation is much smaller. The mean prevailing surface winds are southerly throughout the day and night during the Mei-Yu season, with the wind speed over ocean being much stronger.

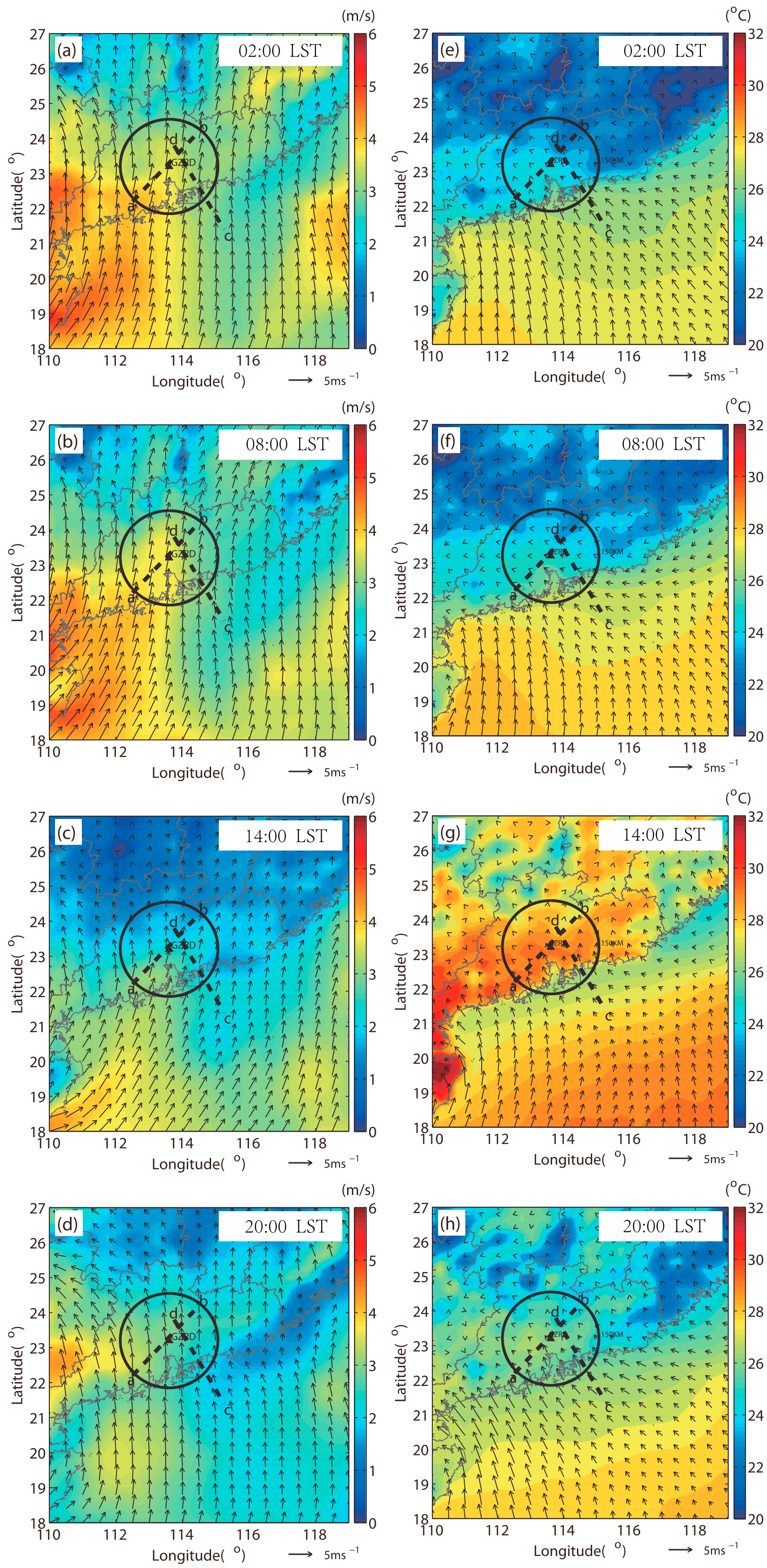

Figure 8. (a–d) Mean wind speed (color-filled contours) and horizontal wind vectors (arrows) at 900 hPa and (e–h) temperature (color-filled contours) and horizontal wind vectors (arrows) at the surface for the 2007–2009 Mei-Yu seasons. Four times of the day are presented from top to bottom at 0200, 0800, 1400, and 2000 LST. The solid circle indicates the range of the radar.

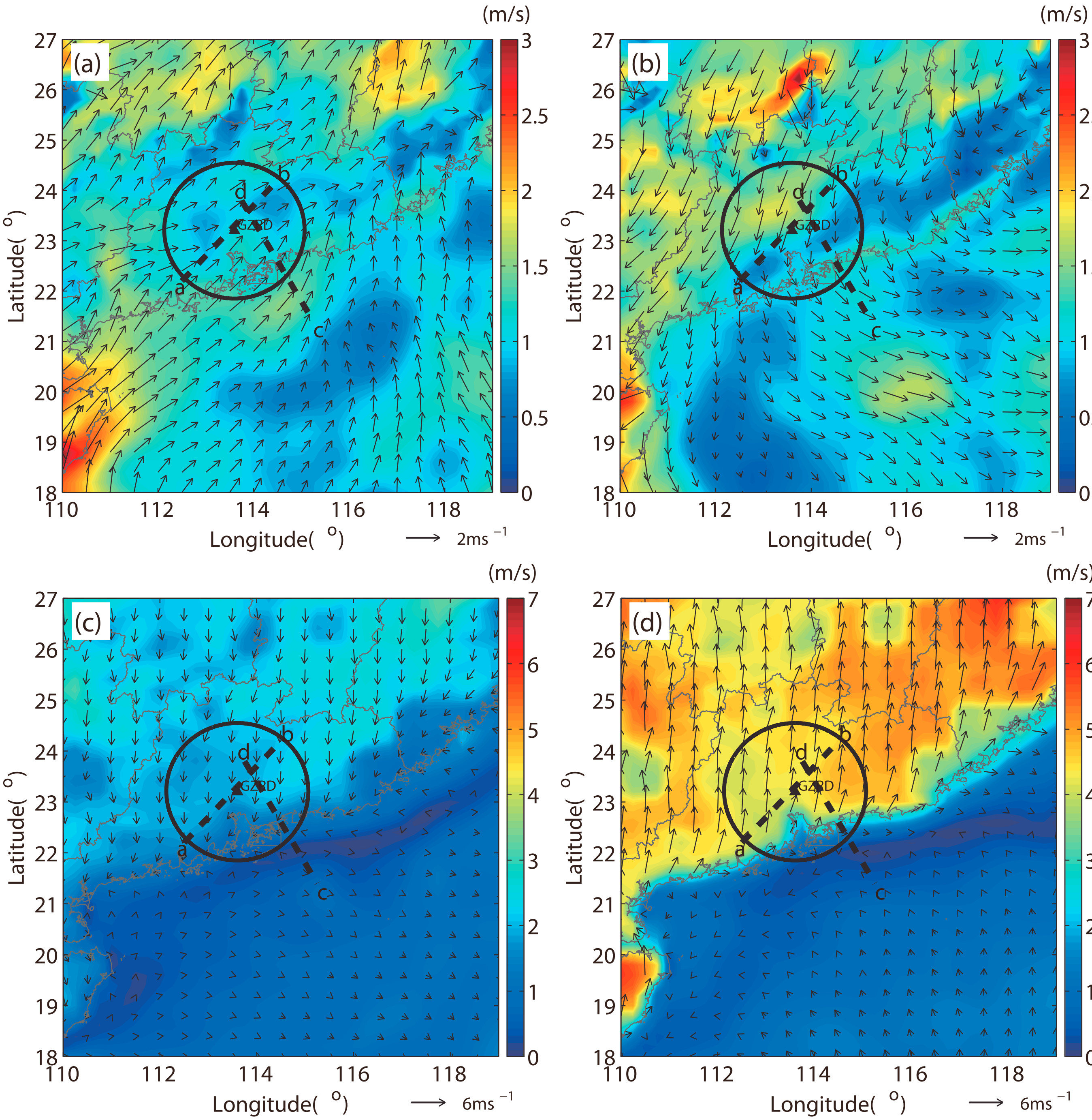

Figure 9. The full wind speed ($\sqrt{(u(t1)\ -\ u(t2))^2\ +\ (v(t1)\ -\ v(t2))^2}$, color-filled contours) and wind vectors (arrows) differences (a and c) between 0200 and 2000 LST and (b and d) between 1400 and 0800 LST at 900 hPa (Figures 9a and 9b) and at the surface (Figures 9c and 9d). Note the differences in the arrow sizes and color bars in Figures 9a and 9b and Figures 9c and 9d.

The diurnal variation in the surface winds is most evident in the difference fields. Between 0200 and 2000 LST, the wind difference is mostly offshore (Figure 9c) over land, indicating the development of land breeze at night. The difference wind vectors between 1400 and 0800 LST are strongly onshore (Figure 9d), due to the development of sea breeze in the afternoon and the surface strengthening of land breeze in the early morning (at 0800 LST). The development of land and sea breezes at different times of the day in response to the land-sea temperature contrast is believed to be related to the nocturnal convective initiation along coastline and inland propagation of convection during the day.

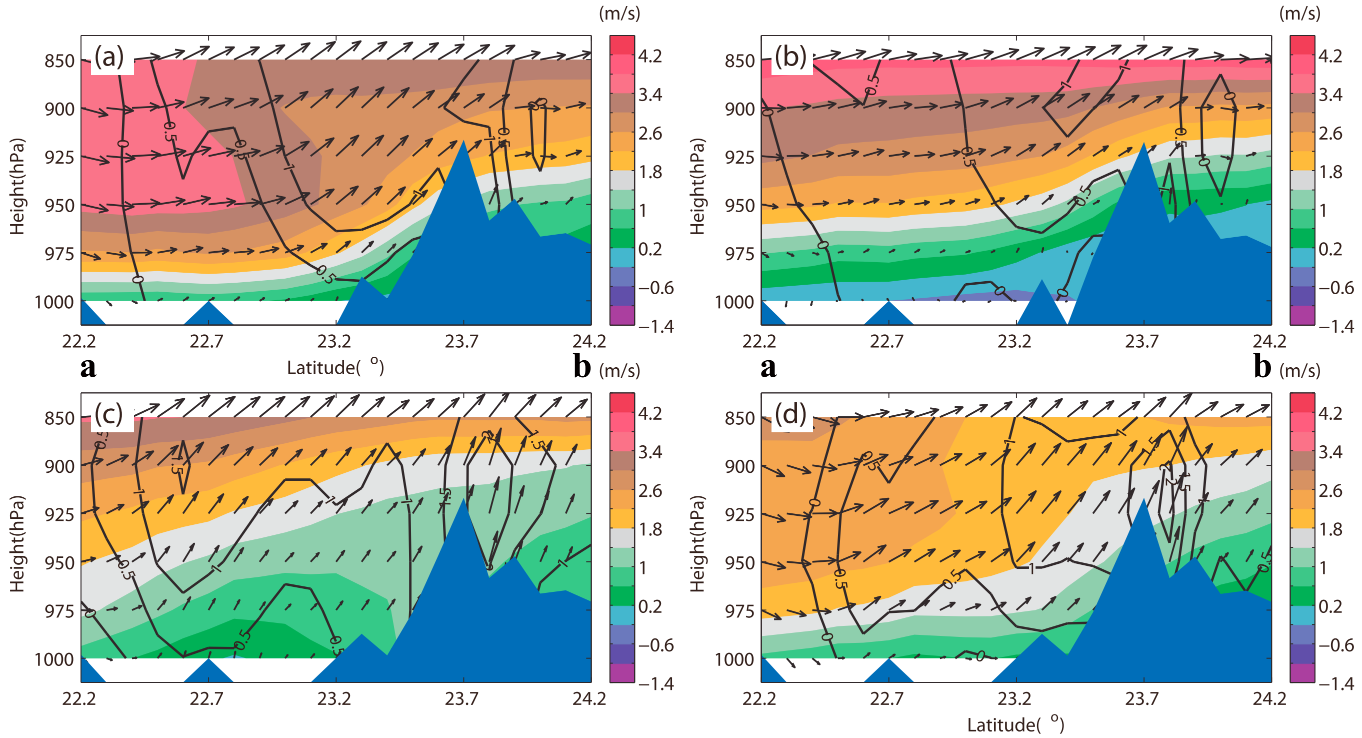

Figure 10. Wind vectors (arrows) along line a-b in Figure 8 and the wind component (color filled) projected to the plane at (a) 0200, (b) 0800, (c) 1400, and (d) 2000 LST. Black contours are for the vertical velocity. The interpolated topographic profiles are shown by blue shading.

4.3.1. Mechanisms of Peak Convection Over the Mountains

Cross sections along the dashed line a-b in Figure 8 at 0200, 0800, 1400, and 2000 LST are shown in Figure 10. The average prevailing winds under 850 hPa are southwesterly to southerly in this region. The horizontal winds between 925 hPa and 975 hPa at nighttime (Figure 10a) are much stronger than that in the afternoon (Figure 10c). Such enhanced nocturnal boundary layer winds are similar to the warm season nocturnal LLJ over the Great Plains of the United States [*Blackadar*, 1957; *Bonner*, 1968; *Mitchell et al.*, 1995; *Zhong et al.*, 1996; *Whiteman et al.*, 1997; *Jiang et al.*, 2007; *Parish and Oolman*, 2010; *Holton*, 2011; *Du and Rotunno*, 2014]. *Blackadar* [1957] proposed that the nocturnal supergeostrophic LLJ is a result of the inertial oscillation of the ageostrophic wind triggered by the sudden decay of eddy viscosity and therefore the effective removal of surface drag on the boundary layer by the ground surface after sunset. The development of southwesterly nocturnal boundary layer jet is more evident in the wind difference fields between early morning and early evening, as shown in Figure 9.

This enhanced nocturnal boundary layer winds can also be seen from long-term ground-based radar observations. Figure 11 presents the hourly averaged 0.5°-elevation radial velocity from the GZRD for the 3 year Mei-Yu seasons. Positive (negative) radial velocity means flow is departing from (moving toward) the radar site. Assuming that the environmental winds are uniform at each height level, the wind speed and direction at a given height can be determined by the extreme Doppler velocity values around a constant slant range circle [*Brown and Wood*, 2007]. Taking into account the Earth curvature effect and radar beam bending, the flows in the blue dashed boxes in Figure 11 are about 800 m above ground level. The environmental winds at this level are dominantly south-southwesterly during the active Mei-Yu period. The average maximum speed of the southwesterly is around 6.5 m s^{-1} in the afternoon (1500–1600 LST) and reaches 10 m s^{-1} in the early morning (0300–0400 LST).

In the vertical cross sections in Figure 10, lifting is strongest in the early afternoon over and behind the mountain peak apparently due to strong solar heating (Figure 10b). Areas of upward motion can clearly be seen during early morning along the windward slope of the mountains, which must be due to the lifting of strong boundary layer flow or LLJ by the mountains (Figure 10d). The lifting of the nocturnal boundary layer LLJ is therefore believed to be responsible for the early morning convection maximum over the mountains, as seen

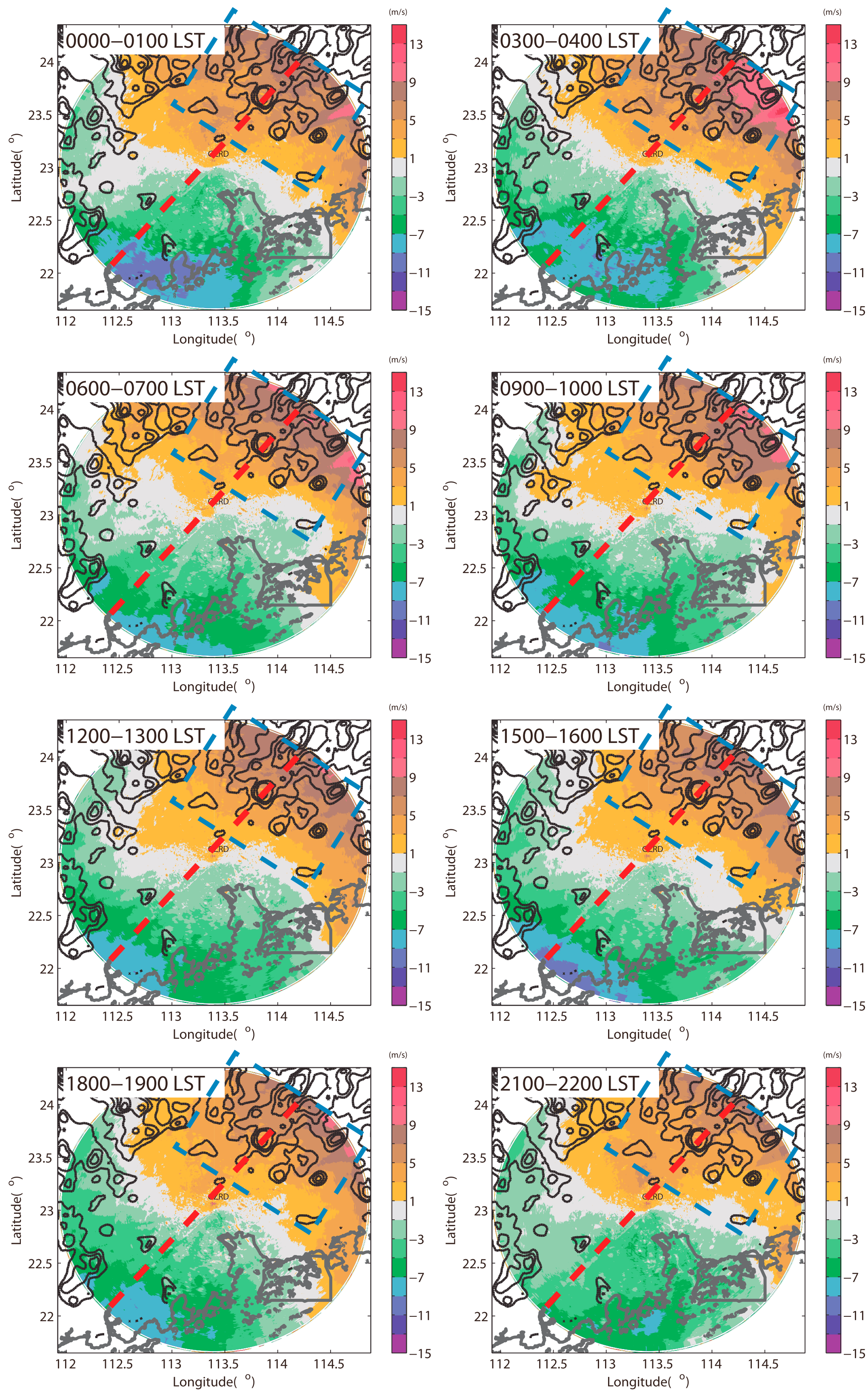

Figure 11. The averaged 0.5° radial velocities from the GZRD at 0000–0100, 0300–0400, 0600–0700, 0900–1000, 1200–1300, 1500–1600, 1800–1900, and 2100–2200 LST during 2007–2009 Mei-Yu seasons. The dash lines a-b in Figure 8 are marked by the red dash lines here.

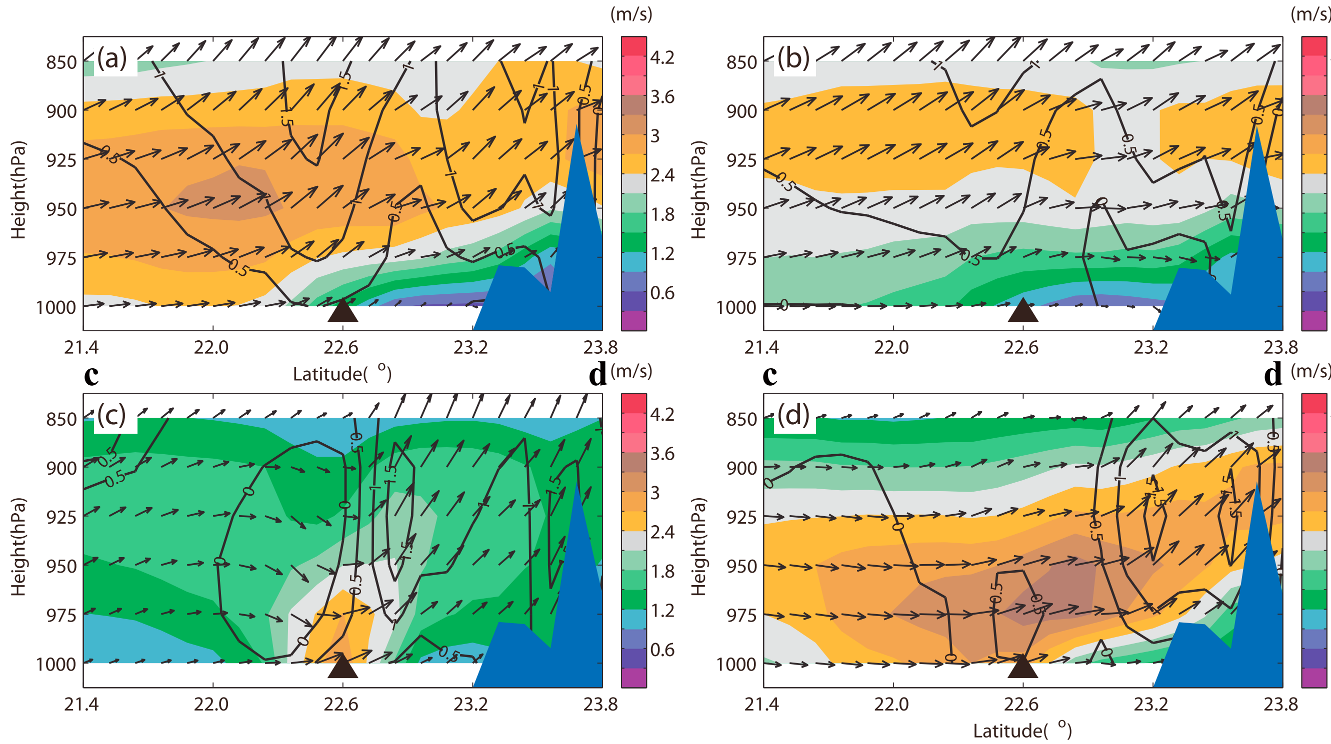

Figure 12. Wind vectors (arrows) along line c-d in Figure 8 and the wind component (color filled) projected to the plane at (a) 0200, (b) 0800, (c) 1400, and (d) 2000 LST. Black contours are for the vertical velocity. The interpolated topographic profiles are shown by blue color. The black triangle indicates the coastline location.

in Figures 5 and 7a. The primary peak of convection in this region in the afternoon is clearly due to maximum solar heating.

4.3.2. Mechanism of the Initiation and Inland Propagation of Convection Near Coastline

Figure 12 shows the cross sections along dashed line c-d in Figure 8, which are roughly normal to the coastline. The location of the coastline is shown by the black triangle. As shown in the figure, the prevailing winds at the low levels are generally onshore. At 0200 LST (Figure 12a), significantly weakened flows are found in the lowest 25 hPa layer beyond ~22.3° in latitude, and this should be due to the land breeze circulation that extends roughly 0.3° offshore. Clearly, the land breeze front creates surface convergence near the front, and correspondingly, rather strong vertical updraft covers the convergence zone (see wind vectors and vertical velocity contours). This land breeze frontal forcing should be the main factor initiating convection near the coast near this time (at and after 0200 LST), which is consistent with the Hovmöller diagram in Figure 7b (even though the Hovmöller diagram shows the mean in the coast-normal direction). Between 0200 and 0800 LST, the near-surface land breeze circulation roughly maintains its strength (Figure 12b), which is consistent with the more or less stationary positioning of the core region of convection during this period seen in Figure 7b. After the initiation off the coast, there is general tendency for inland propagation of the convection, which becomes more pronounced after sunrise (Figure 7b). This is consistent with the weakening of land breeze circulation and the subsequent development of sea breeze and the inland propagation of sea breeze front, as well as the presence of generally southerly prevailing winds. By 1400 LST (Figure 12c), the sea breeze front appears to be about 0.3° inland, and there is a broad updraft between the sea breeze front and the mountains. With intense solar heating in the afternoon, and perhaps with the help of sea breeze circulation also, convection in Figure 7b reaches maximum at around 1400 LST. After 1600 LST, convection dies out (Figure 7b), apparently due to the weakening of both solar heating and sea breeze circulation. These results suggest that the initial initiation of convection after midnight near the coast is primarily caused by the development of land breeze, while the subsequent inland propagation of convection, as seen in Figure 7b, is primarily caused by the inland propagation of sea breeze front, as well as by the inland advection of prevailing winds. Deep inland propagation of sea breeze front by prevailing wind from the Gulf of Mexico coast to as far as central Texas is recently documented by *Hu and Xue* [2015]. The elevated heating over the mountains in the region appears to have also played a role in the afternoon precipitation maximum as seen in Figure 7b.

5. Summary and Conclusions

The Pearl River Delta (PRD) region, one of the most important economic and population centers in China, is also a climatological rainfall center in South China. During the Mei-Yu season, also known as the presummer rainy season of South China by Chinese meteorologists, heavy precipitation leads to loss of life and property and urban inundation almost every year. In the region, convective rainfall accounts for more than 70% of the total rainfall during the Mei-Yu season. However, prediction of convective rainfall in the region is still a big challenge, while a good understanding of the mechanisms behind the diurnal evolution of convection in the region is still lacking.

In this paper, the diurnal cycle and propagation of convection over PRD during the Mei-Yu season are studied using data from operational weather radar for 3 years. Sounding data and JMA gridded reanalysis data are used to examine the mean meteorological conditions, including flow patterns and thermodynamic properties. Different from earlier studies based on polar-orbiting satellite data, this paper takes advantage of the high temporal and spatial resolutions of ground-based radars to reveal detailed variations in diurnal cycle and propagation over PRD during the Mei-Yu seasons.

Convective grid point is first identified based on the radar reflectivity data. Precipitation is also estimated from the reflectivity data. During Mei-Yu seasons, two main centers of high convection frequency are found in the PRD region. One is on the windward slope of the mountains in the northeastern part of the region (region B), and the other is along the southern coastline (region C). A frequency minimum is found in the western part of the PRD (region A).

Convection shows clear and different diurnal cycles in the three subregions (regions A–C). Region A has the most prominent, single afternoon peak throughout the day. Region B has a primary peak in the early afternoon and a secondary peak in the early morning. Region C has a single peak around noon, and convection in this region starts to initiate at night. The Hovmöller diagram of convective propagation in region B shows that both early morning and early afternoon convection are triggered locally on the windward slope of northeastern mountains. The Hovmöller diagram perpendicular to the coastline shows a clear inland propagation trend form early morning to early afternoon. From the radial velocity data and JMA reanalysis data, early morning convection in region B is shown to be closely related to the nocturnal acceleration of southwesterly boundary layer flow. Early morning convection in region C is believed to be triggered by the convergence between land breeze and the prevailing onshore winds near the coastline.

We note here that in the Mei-Yu season of southern China, there is, in general, frequent precipitation from mesoscale convection systems which tends to damp the solar heating reaching the ground. The fact that strong afternoon heating still has important effects on the diurnal cycles of precipitation in the PRD region is by itself interesting. The afternoon heating has several roles: first is to directly promote afternoon precipitation maximum, especially over the mountain regions, the second is to retard the boundary layer flow over land in the afternoon to set the stage for the development of nocturnal (supergeostrophic) boundary layer jet via the Blackadar inertial oscillation mechanism, and the third effect is to set up land-sea temperature gradients for land and sea breeze circulations to develop, which tend to produce convective systems that propagate relative to the coastline.

We noted that in C14, it was found based on 3 years of radar data spanning the warm season months of May through September that precipitation is predominantly found along the PRD coastline on days with a synoptic southerly LLJ, while on non-LLJ days, precipitation maxima are found both along the coastline and over the northeastern mountains. Differential friction-induced low-level convergence was proposed to be the cause of coastal precipitation maximum on LLJ days. For the days included in the Mei-Yu seasons of this study and based on the same criteria used by C14, only 19 days had LLJ, while 116 days are non-LLJ days. For this reason, differential friction only plays a partial role during the Mei-Yu seasons studied here, while the land and sea breeze circulations play important roles in the initiation and propagation of convection in the PRD region. In addition, the propagation and related mechanisms of well-organized and long-lived convective systems over PRD also require further investigation as was done in *Carbone et al.* [2002].

Finally, we note that studies such as *Luo et al*. [2013] had examined precipitation climatology in the Yangtze River-Huaihe region, into which Mei-Yu frontal system moves at the end of the southern China Mei-Yu season, although most of such studies used much less frequent precipitation data, such as those from TRMM satellites. It would be interesting to study precipitation climatology in the Yangtze River-Huaihe region using the ground-based radar data with much higher temporal and spatial resolutions and compare the precipitation characteristics among the regions. Such efforts are ongoing.

Acknowledgments
This work was primarily supported the National Basic Research Program of China (973 program; 2013CB430101) and Special Fund for Public Welfare Industry (Meteorology) of China (GYHY201006007), the National Natural Science Foundation of China (grants 41275031 and 41322032), and Program for New Century Excellent Talents in University of China. Observational data used in this study were collected by the National Basic Research Program of China (973 program; 2013CB430101). Special requests for the data can be made at http://scw973.nju.edu.cn/ or contacting the project office at yang.zhengwei@nju.edu.cn. After 2018, the data of this paper will be uploaded to http://www.nersc.gov/users/science-gate-ways/ for public sharing. We also thank the Editor and three anonymous reviewers for their valuable suggestions that improved our paper.

References

Astling, E. G., J. Paegle, E. Miller, and C. J. O'Brien (1985), Boundary layer control of nocturnal convection associated with a synoptic scale system, *Mon. Weather Rev.*, *113*(4), 540–552.

Bao, X., F. Zhang, and J. Sun (2011), Diurnal variations of warm-season precipitation east of the Tibetan Plateau over China, *Mon. Weather Rev.*, *139*(9), 2790–2810.

Blackadar, A. K. (1957), Boundary layer wind maxima and their significance for the growth of nocturnal inversions, *Bull. Am. Meteorol. Soc.*, *38*, 283–290.

Bonner, W. D. (1968), Climatology of the low level jet, *Mon. Weather Rev.*, *96*(12), 833–850.

Brown, R. A., and V. T. Wood (2007), *A Guide for Interpreting Doppler Velocity Patterns: Northern Hemisphere Edition*, 55 pp., NOAA/Natl. Severe Storms Lab. Norman, Okla.

Carbone, R. E., and J. D. Tuttle (2008), Rainfall occurrence in the U.S. warm season: The diurnal cycle, *J. Clim.*, *21*(16), 4132–4146.

Carbone, R. E., J. W. Wilson, T. D. Keenan, and J. M. Hacker (2000), Tropical island convection in the absence of significant topography. Part I: Life cycle of diurnally forced convection, *Mon. Weather Rev.*, *128*(10), 3459–3480.

Carbone, R. E., J. D. Tuttle, D. A. Ahijevych, and S. B. Trier (2002), Inferences of predictability associated with warm season precipitation episodes, *J. Atmos. Sci.*, *59*(13), 2033–2056.

Chang, P.-L., P.-F. Lin, B. Jong-Dao Jou, and J. Zhang (2009), An application of reflectivity climatology in constructing radar hybrid scans over complex terrain, *J. Atmos. Oceanic Technol.*, *26*(7), 1315–1327.

Chen, C., W.-K. Tao, P.-L. Lin, G. S. Lai, S. F. Tseng, and T.-C. C. Wang (1998), The intensification of the low-level jet during the development of mesoscale convective systems on a Mei-Yu front, *Mon. Weather Rev.*, *126*(2), 349–371.

Chen, G., W. Sha, and T. Iwasaki (2009), Diurnal variation of precipitation over southeastern China: Spatial distribution and its seasonality, *J. Geophys. Res.*, *114*, D13103, doi:10.1029/2008JD011103.

Chen, G. T.-J., and C.-C. Yu (1987), Study of low-level jet and extremely heavy rainfall over Northern Taiwan in the Mei-Yu season, *Mon. Weather Rev.*, *116*, 884–891.

Chen, G. T.-J., C.-C. Wang, and D. T.-W. Lin (2004), Characteristics of low-level jets over Northern Taiwan in Mei-Yu season and their relationship to heavy rain events, *Mon. Weather Rev.*, *133*, 20–43.

Chen, H., R. Yu, J. Li, W. Yuan, and T. Zhou (2010), Why nocturnal long-duration rainfall presents an eastward-delayed diurnal phase of rainfall down the Yangtze River Valley, *J. Clim.*, *23*(4), 905–917.

Chen, M., Y. Wang, F. Gao, and X. Xiao (2012), Diurnal variations in convective storm activity over contiguous North China during the warm season based on radar mosaic climatology, *J. Geophys. Res.*, *117*, D20115, doi:10.1029/2012JD018158.

Chen, M., Y. Wang, F. Gao, and X. Xiao (2014a), Diurnal evolution and distribution of warm-season convective storms in different prevailing wind regimes over contiguous North China, *J. Geophys. Res. Atmos.*, *119*, 2742–2763, doi:10.1002/2013JD021145.

Chen, T.-J. G., and C.-P. Chang (1980), The structure and vorticity budget of an early summer monsoon trough (Mei-Yu) over southeastern China and Japan, *Mon. Weather Rev.*, *108*(7), 942–953.

Chen, X., K. Zhao, and M. Xue (2014b), Spatial and temporal characteristics of warm season convection over Pearl River Delta region, China, based on 3 years of operational radar data, *J. Geophys. Res. Atmos.*, *119*, 12,447–12,465, doi:10.1002/2014JD021965.

Chen, Y.-L. (1993), Some synoptic-scale aspects of the surface fronts over southern China during TAMEX, *Mon. Weather Rev.*, *121*(1), 50–64.

Chen, Y.-L., and J. Feng (1995), The influences of inversion height on precipitation and airflow over the island of Hawaii, *Mon. Weather Rev.*, *123*(6), 1660–1676.

Cho, H.-R., and G. T. J. Chen (1995), Mei-Yu frontogenesis, *J. Atmos. Sci.*, *52*(11), 2109–2120.

Ding, Y., and J. C. L. Chan (2005), The East Asian summer monsoon: An overview, *Meteorol. Atmos. Phys.*, *89*(1–4), 117–142.

Ding, Y. H. (1994), *Monsoons Over China*, 419 pp., Kluwer Acad., Dordrecht, Netherlands.

Du, Y., and R. Rotunno (2014), A simple analytical model of the nocturnal low-level jet over the Great Plains of the United States, *J. Atmos. Sci.*, *71*(10), 3674–3683.

He, H., and F. Zhang (2010), Diurnal variations of warm-season precipitation over northern China, *Mon. Weather Rev.*, *138*(4), 1017–1025.

Holton, J. R. (2011), The diurnal boundary layer wind oscillation above sloping terrain, *Tellus A*, *19*(2), 199–205.

Hu, X., and M. Xue (2015), Influence of synoptic sea breeze fronts on the urban heat island intensity in Dallas-Fort Worth, Texas, *Mon. Weather Rev.*, doi:10.1175/MWR-D-15-0201.1.

Iwasaki, H., T. Nii, T. Sato, F. Kimura, K. Nakagawa, I. Kaihotsu, and T. Koike (2008), Diurnal variation of convective activity and precipitable water around Ulaanbaator, Mongolia, and the impact of soil moisture on convective activity during nighttime, *Mon. Weather Rev.*, *136*(4), 1401–1415.

Jiang, X., N.-C. Lau, I. M. Held, and J. J. Ploshay (2007), Mechanisms of the Great Plains low-level jet as simulated in an AGCM, *J. Atmos. Sci.*, *64*(2), 532–547.

Johnson, R. H., and P. E. Ciesielski (2002), Characteristics of the 1998 summer monsoon onset over the Northern South China Sea, *J. Meteorol. Soc. Jpn. Ser. II*, *80*(4), 561–578.

Johnson, R. H., P. E. Ciesielski, T. S. L'Ecuyer, and A. J. Newman (2010), Diurnal cycle of convection during the 2004 North American Monsoon Experiment, *J. Clim.*, *23*(5), 1060–1078.

Jou, B. J.-D., and S.-M. Deng (1998), The organization of convection in a Mei-Yu frontal rainband, *TAO*, *9*, 553–572.

Lang, T. J., D. A. Ahijevych, S. W. Nesbitt, R. E. Carbone, S. A. Rutledge, and R. Cifelli (2007), Radar-observed characteristics of precipitating systems during NAME 2004, *J. Clim.*, *20*(9), 1713–1733.

Liu, P., and Y. Fu (2010), Climatic characteristics of summer convective and stratiform precipitation in southern China based on measurement by TRMM precipitation radar [in Chinese], *Chin. J. Atmos. Sci.*, *34*(4), 802–814.

Luo, Y., H. Wang, R. Zhang, W. Qian, and Z. Luo (2013), Comparison of rainfall characteristics and convective properties of monsoon precipitation systems over South China and the Yangtze and Huai River Basin, *J. Clim.*, *26*(1), 110–132.

Marshall, J. S., and W. M. K. Palmer (1948), The distribution of raindrops with size, *J. Meteorol.*, *5*(4), 165–166.

Mitchell, M. J., R. W. Arritt, and K. Labas (1995), A climatology of the warm season Great Plains low-level jet using wind profiler observations, *Weather Forecast.*, *10*(3), 576–591.

Mohr, C. G., and R. L. Vaughan (1979), An economical procedure for Cartesian interpolation and display of reflectivity factor data in three-dimensional space, *J. Appl. Meteorol.*, *18*(5), 661–670.

Nesbitt, S. W., and E. J. Zipser (2003), The diurnal cycle of rainfall and convective intensity according to three years of TRMM measurements, *J. Clim.*, *16*(10), 1456–1475.

Parish, T. R., and L. D. Oolman (2010), On the role of sloping terrain in the forcing of the Great Plains low-level jet, *J. Atmos. Sci.*, *67*(8), 2690–2699.

Parker, M. D., and J. C. Knievel (2005), Do meteorologists suppress thunderstorms?: Radar-derived statistics and the behavior of moist convection, *Bull. Am. Meteorol. Soc.*, *86*(3), 341–358.

Rodwell, M. J., and B. J. Hoskins (2001), Subtropical anticyclones and summer monsoons, *J. Clim.*, *14*(15), 3192–3211.

Romatschke, U., and R. A. Houze (2011), Characteristics of precipitating convective systems in the South Asian monsoon, *J. Hydrometeorol.*, *12*(1), 3–26.

Romatschke, U., S. Medina, and R. A. Houze (2010), Regional, seasonal, and diurnal variations of extreme convection in the South Asian region, *J. Clim.*, *23*(2), 419–439.

Saito, K., et al. (2006), The operational JMA nonhydrostatic mesoscale model, *Mon. Weather Rev.*, *134*(4), 1266–1298.

Steiner, M., R. A. H. Houze Jr., and S. E. Yuter (1995), Climatological characterization of three-dimensional storm structure form operational radar and rain gauge data, *J. Appl. Meteorol.*, *34*(9), 1978–2007.

Sun, J., and F. Zhang (2011), Impacts of mountain–plains solenoid on diurnal variations of rainfalls along the Mei-Yu front over the East China Plains, *Mon. Weather Rev.*, *140*(2), 379–397.

Wallace, J. M. (1975), Diurnal variations in precipitation and thunderstorm frequency over the conterminous United States, *Mon. Weather Rev.*, *103*(5), 406–419.

Wang, H., Y. Luo, and B. J.-D. Jou (2014), Initiation, maintenance, and properties of convection in an extreme rainfall event during SCMREX: Observational analysis, *J. Geophys. Res. Atmos.*, *119*, 13,206–13,232, doi:10.1002/2014JD022339.

Watson, A. I., R. E. López, and R. L. Holle (1994), Diurnal cloud-to-ground lightning patterns in Arizona during the southwest monsoon, *Mon. Weather Rev.*, *122*(8), 1716–1725.

Whiteman, C. D., X. Bian, and S. Zhong (1997), Low-level let climatology from enhanced rawinsonde observations at a site in the Southern Great Plains, *J. Appl. Meteorol.*, *36*(10), 1363–1376.

Xu, W., and E. J. Zipser (2011), Diurnal variations of precipitation, deep convection, and lightning over and east of the Eastern Tibetan Plateau, *J. Clim.*, *24*(2), 448–465.

Xu, W., E. J. Zipser, and C. Liu (2009), Rainfall characteristics and convective properties of Mei-Yu precipitation systems over South China, Taiwan, and the South China Sea. Part I: TRMM observations, *Mon. Weather Rev.*, *137*(12), 4261–4275.

Xu, X., K. Howard, and J. Zhang (2008), An automated radar technique for the identification of tropical precipitation, *J. Hydrometeorol.*, *9*(5), 885–902.

Yang, G.-Y., and J. Slingo (2001), The diurnal cycle in the tropics, *Mon. Weather Rev.*, *129*(4), 784–801.

Yang, S., and E. A. Smith (2008), Convective–stratiform precipitation variability at seasonal scale from 8 yr of TRMM observations: Implications for multiple modes of diurnal variability, *J. Clim.*, *21*(16), 4087–4114.

Yu, R., T. Zhou, A. Xiong, Y. Zhu, and J. Li (2007), Diurnal variations of summer precipitation over contiguous China, *Geophys. Res. Lett.*, *34*, L01704, doi:10.1029/2006GL028129.

Yu, R., W. Yuan, J. Li, and Y. Fu (2010), Diurnal phase of late-night against late-afternoon of stratiform and convective precipitation in summer southern contiguous China, *Clim. Dyn.*, *35*(4), 567–576.

Yuan, W., R. Yu, M. Zhang, W. Lin, J. Li, and Y. Fu (2012), Diurnal cycle of summer precipitation over subtropical East Asia in CAM5, *J. Clim.*, *26*(10), 3159–3172.

Zhang, J., and S. Wang (2006), An automated 2D multipass Doppler radar velocity dealiasing scheme, *J. Atmos. Oceanic Technol.*, *23*, 1239–1248.

Zhang, J., S. Wang, and B. Clarke (2004), WSR-88D reflectivity quality control using horizontal and vertical reflectivity structure, paper presented at Preprints, 11th Conf. Aviation, Range, and Aerospace Meteorol., Am. Meteorol. Soc., Hyannis, Mass.

Zhao, Y. (2013), Diurnal variation of rainfall associated with tropical depression in South China and its relationship to land-sea contrast and topography, *Atmosphere*, *5*(1), 16–44.

Zhong, S., J. D. Fast, and X. Bian (1996), A case study of the Great Plains low-level jet using wind profiler network data and a high-resolution mesoscale model, *Mon. Weather Rev.*, *124*(5), 785–806.